

An unidentified line in X-ray spectra of the Andromeda galaxy and Perseus galaxy cluster

A. Boyarsky¹, O. Ruchayskiy², D. Iakubovskiy^{3,4} and J. Franse^{1,5}

¹Instituut-Lorentz for Theoretical Physics, Universiteit Leiden, Niels Bohrweg 2, Leiden, The Netherlands

²Ecole Polytechnique Fédérale de Lausanne, FSB/ITP/LPPC, BSP, CH-1015, Lausanne, Switzerland

³Bogolyubov Institute of Theoretical Physics, Metrologichna Str. 14-b, 03680, Kyiv, Ukraine

⁴National University “Kyiv-Mohyla Academy”, Skovorody Str. 2, 04070, Kyiv, Ukraine

⁵Leiden Observatory, Leiden University, Niels Bohrweg 2, Leiden, The Netherlands

We report a weak line at 3.52 ± 0.02 keV in X-ray spectra of M31 galaxy and the Perseus galaxy cluster observed by MOS and PN cameras of XMM-Newton telescope. This line is not known as an atomic line in the spectra of galaxies or clusters. It becomes stronger towards the centers of the objects; is stronger for Perseus than for M31; is absent in the spectrum of a deep “blank sky” dataset. Although for each object it is hard to exclude that the feature is due to an instrumental effect or an atomic line, it is consistent with the behavior of a dark matter decay line. Future (non-)detections of this line in multiple objects may help to reveal its nature.

The nature of dark matter (DM) is a question of crucial importance for both cosmology and for fundamental physics. As neutrinos – the only known particles that could be DM candidates – are too light to be consistent with various observations [1–4], it is widely anticipated that new particles should exist. Although many candidates have been put forward (see e.g. [5]), little is known experimentally about the properties of DM particles: their masses, lifetimes, and interaction types remain largely unconstrained. *A priori*, a given DM candidate can possess a decay channel if its lifetime exceeds the age of the Universe. Therefore, the search for a DM decay signal provides an important test to constrain the properties of DM in a model-independent way. For fermionic particles, one should search above the Tremaine-Gunn limit [1] ($\gtrsim 300$ eV). If the mass is below $2m_e c^2$, such a fermion can decay to neutrinos and photons with energy $E_\gamma = \frac{1}{2}m_{\text{DM}}$ [6]. One can search for such particles in X-rays [7, 8] (see [9] for review of previous searches). For each particular model, the particle’s parameters are related by the requirement to provide the correct DM abundance. For example, for one very interesting DM candidate – the right-handed neutrino – this requirement restricts the mass range to 0.5 – 100 keV [9, 10]. A large part of the available parameter space for sterile neutrinos is consistent with all astrophysical and cosmological bounds [11], and it is important to probe it further.

The DM decay line is much narrower than the spectral resolution of the existing X-ray telescopes and, as previous searches have shown, should be rather weak. The X-ray spectra of astrophysical objects are crowded with weak atomic and instrumental lines, not all of which may be known. Therefore, even if the exposure of available observations continues to increase, it is hard to exclude an astrophysical or instrumental origin of any weak line found in the spectrum of individual object. However, if the same feature is present in the spectra of many different objects, and its surface brightness and relative normalization between objects are consistent with the expected behavior of the DM signal, this can provide much more convincing evidence about its nature.

The present paper takes a step in this direction. We present the results of the combined analysis of many *XMM-Newton* observations of two objects at different redshifts – the Perseus cluster ($z = 0.0179$ [12]) and the Andromeda galaxy (M31, $z = -0.001$)¹, a Local Group member – together with a long exposure “blank sky” dataset. We present the detection of a significant un-modeled excess at 3.52 ± 0.02 keV (restframe) in both objects. We study its behaviour and establish that it is consistent with a DM interpretation. However, as the line is weak ($\sim 4\sigma$ in the combined dataset) and the uncertainties in DM distribution are significant, positive detections or strong constraints from more objects are clearly needed to determine its nature.²

Below we summarize the details of our data analysis and then discuss the results and caveats.

Data analysis. We use the data obtained with MOS [19] and PN [20] CCD cameras of *XMM-Newton* (“XMM” in what follows). We use SAS v.13.0.0 [21] to reduce the raw data and filter the data for *soft solar protons* [22, 23] using the `espsfilt` procedure. Because residual soft proton flares can produce weak line-like features in the spectra at positions where the effective area is non-monotonic (see e.g. [24]), we apply the procedure described in [25], based on the comparison of high-energy count rates for “in-FoV” (10-15 arcmin off-center) and out-FoV CCD regions [26]. We selected only observations where the ratio of $F_{in} - F_{out} < 1.15$.³

¹ Each of the datasets used in previous decaying DM searches in M31 [13–17] had less statistics than we use. The non-detection of any signal in these works does not come in contradiction with our results.

² When this paper was in preparation, the arXiv preprint of [18] appeared, claiming a detection of a spectral feature at the same energy from a collection of galaxy clusters. Our analyses are independent, based on different datasets, but the results are fully consistent.

³ Ref. [25] argued that $F_{in} - F_{out} < 1.3$ is a sufficient criterion for flare removal. We find by visual inspection of the resulting spectra that a stricter criterion is needed to reduce artificial line-like residuals [24, 27]. Lowering

Combined observation of M31. We use ~ 2 Msec of raw exposure observations of M31 within the central 1.5° (see SOM, Table II). We select from the XMM archive 29 MOS observations offset less than $1.5'$ from the center of M31, and 20 MOS observations with offsets $23.7' - 55.8'$ that passed our criterion for residual contamination. Not enough PN observations passed this test to include them. The central and off-center observations were co-added separately with the `addspec` routine from `FTOOLS` [28]. The resulting spectra were binned by 60 eV. This bin size is a factor ~ 2 smaller than the spectral resolution of the XMM at these energies, which makes the bins roughly statistically independent.

Background modeling. We model the contribution of the instrumental (particle induced) background by a combination of an unfolded power law plus several narrow `gaussian` lines. The positions and normalizations of the lines were allowed to vary freely and the most prominent instrumental $K\text{-}\alpha$ lines (Cr, Mn, K, Fe, Ni, Ca, Cu) and Fe $K\beta$ have been recovered. The width of the Gaussians was fixed at 1 eV (an infinitely thin line for the XMM spectral resolution). We verified that allowing the line widths to vary freely leaves the results unchanged. We restrict our modeling to the energy interval 2–8 keV. The Galactic foreground is negligible above 2 keV [29]. The combined emission of unresolved point sources at these energies is modeled by a `powerlaw` [30]. Several line-like residuals around 2.4 keV and 3.0 keV were identified as Ar and S line complexes and the corresponding thin (1 eV width) lines were added to the model. We verified that adding another `powerlaw` component to model the contribution of the extragalactic X-ray background [25, 29] does not improve the quality of fit and does not change the structure of the residuals.

Result. The resulting spectrum of the central observations shows a group of positive residuals around 3.5 keV (Fig. 1). Adding a thin Gaussian line at that energy reduces the total χ^2 by ~ 13 , see Table I (more than 3σ significance for extra 2 degrees of freedom). Examination of MOS1 and MOS2 observations individually finds the line in both cameras with comparable flux. For the off-center observations, none of the cameras show any detectable residual in the energy range 3.50 – 3.56 keV. The 2σ upper bound on the flux is given in Table I.

Perseus cluster. If the candidate weak signal is of astrophysical (rather than instrumental) origin, we should be able to detect its redshift. To this end we have chosen the nearby Perseus cluster (Abell 426). At its redshift the line’s centroid would be shifted by 63 eV. As the position of the line is deter-

mined with about 30 eV precision, one can expect to resolve the line’s shift with about 2σ significance.

We took 16 off-center observations of the Perseus cluster (SOM, Table II) and processed them in the same way as for M31. The flare removal procedure left 215 ksec of PN camera’s exposure, therefore we also use PN data.

Background modeling. The resulting spectra were then added together and fitted to the combination of `vmekal` (with free abundances for Fe, Ni, Ar, Ca and S) plus (extragalactic) `powerlaw`. The instrumental background was modeled as in the M31 case.

Results. The fit shows significant positive residuals at energies around 3.47 keV (in the detector frame). Adding a `zgauss` model with the redshift of the cluster improves the fit by $\Delta\chi^2 = 9.1$. The line’s position is fully consistent with that of M31 (Table I). If we fix the position of the line to that of M31 and allow the redshift to vary, $z = 0$ provides a worse fit by $\Delta\chi^2 = 3.6$ and its best-fit value is $(1.73 \pm 0.08) \times 10^{-2}$ – close to the value $z = 0.0179$ which we have used.

Blank-sky dataset. To further study the origin of the new line and possible systematic effects we combine XMM blank-sky observations from [31, 32] with observations of the Lockman Hole [33]. The data were reduced similarly to the other datasets. Fig. 3 shows the combined spectrum. A dataset with such a large exposure requires special analysis (as described in [27]). This analysis did not reveal any line-like residuals in the range 3.45 – 3.58 keV with the 2σ upper bound on the flux being 7×10^{-7} cts/cm²/sec. The closest detected line-like feature ($\Delta\chi^2 = 4.5$) is at $3.67_{-0.05}^{+0.10}$ keV, consistent with the instrumental Ca $K\alpha$ line.⁴

Combined fit of M31 + Perseus. Finally, we have performed a simultaneous fit of the on-center M31 and Perseus datasets (MOS), keeping a common position of the line (in the rest-frame) and allowing the line normalizations to be different. The line improves the fit by $\Delta\chi^2 = 25.9 - 4.4\sigma$ significance (Table I).

Results and discussion. We identified a spectral feature at $E = 3.52 \pm 0.02$ keV in the combined dataset of M31 and Perseus with a statistical significance 4.4σ which does not coincide with any known line. Next we compare its properties with the expected behavior of a DM decay line.

The observed brightness of a decaying DM should be proportional to its column density $\mathcal{S}_{\text{DM}} = \int \rho_{\text{DM}} dl$ – integral along the line of sight of the DM density distribution – and inversely

⁴ Previously this line has only been observed in the PN camera [20].

the threshold further is not feasible as the statistical errorbars on the value of $F_{\text{in}} - F_{\text{out}}$ are of the order of 5%.

Dataset	Exposure [ksec]	$\chi^2/\text{d.o.f.}$	Line position [keV]	Flux [10^{-6} cts/sec/cm 2]	$\Delta\chi^2$	Significance
M31 ON-CENTER	978.9	97.8/74	3.53 ± 0.03	$4.9^{+1.6}_{-1.3}$	13.0	3.2σ
M31 OFF-CENTER	1472.8	107.8/75	3.50 – 3.56	$< 1.8 (2\sigma)$...	
PERSEUS CLUSTER (MOS)	628.5	72.7/68	3.50 ± 0.04	$7.0^{+2.6}_{-2.6}$	9.1	2.6σ
PERSEUS CLUSTER (PN)	215.5	62.6/62	3.46 ± 0.04	$9.2^{+3.1}_{-3.1}$	8.0	2.4σ
PERSEUS (MOS)	1507.4	191.5/142	3.52 ± 0.02	$8.6^{+2.2}_{-2.3}$ (Perseus)	25.9	4.4σ
+ M31 ON-CENTER				$4.6^{+1.4}_{-1.4}$ (M31)	(3 dof)	
BLANK-SKY	15700.2	33.1/33	3.45 – 3.58	$< 0.7 (2\sigma)$...	

TABLE I: Basic properties of combined observations used in this paper. Second column denotes the sum of exposures of individual observations. The improvement in $\Delta\chi^2$ when extra line is added to a model is quoted for each dataset. The last column shows the local significance of such an improvement when 2 extra d.o.f. (position and flux of the line) are added. The energies for Perseus are quoted in the rest frame. Taking into account trial factors, the global (over three datasets) significance is 4.4σ (see SOM for details).

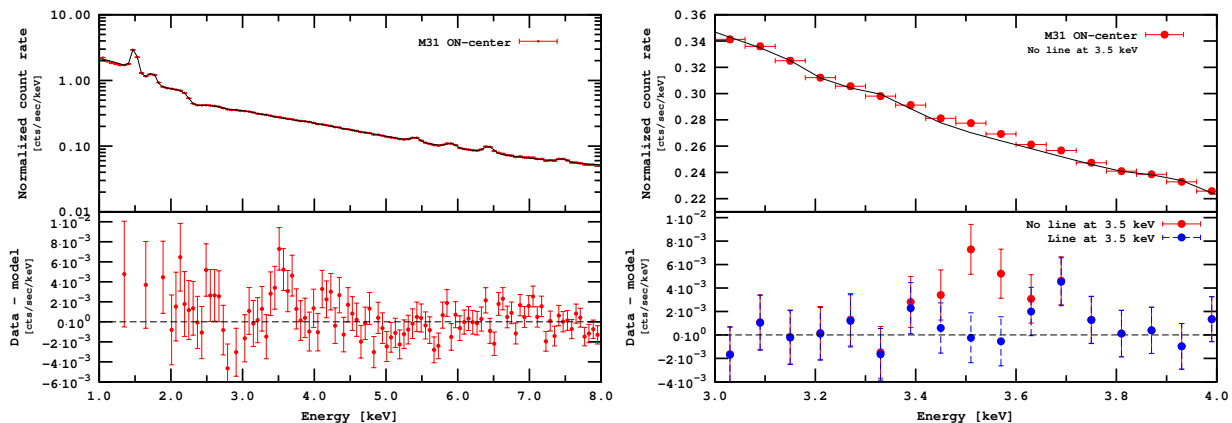


FIG. 1: *Left*: Folded count rate (top) and residuals (bottom) for the MOS spectrum of the central region of M31. Statistical Y-errorbars on the top plot are smaller than the point size. The line around 3.5 keV is *not added*, hence the group of positive residuals. *Right*: zoom onto the line region.

proportional to the radiative decay lifetime τ_{DM} :

$$F_{\text{DM}} \approx 2.0 \times 10^{-6} \frac{\text{cts}}{\text{cm}^2 \cdot \text{sec}} \left(\frac{\Omega_{\text{fov}}}{500 \text{ arcmin}^2} \right) \times \left(\frac{\mathcal{S}_{\text{DM}}}{500 M_{\odot}/\text{pc}^2} \right) \frac{10^{29} \text{ s}}{\tau_{\text{DM}}} \left(\frac{\text{keV}}{m_{\text{DM}}} \right). \quad (1)$$

M31 and Perseus brightness profiles. Using the line flux of the center of M31 and the upper limit from the off-center observations we constrain the spatial profile of the line. The DM distribution in M31 has been extensively studied (see an overview in [24]). We take NFW profiles for M31 with concentrations $c = 11.7$ (solid line, [34]) and $c = 19$ (dash-dotted line). For each concentration we adjust the normalization so it passes through first data point (Fig. 2). The $c = 19$ profile was chosen to intersect the upper limit, illustrating that the obtained line fluxes of M31 are fully consistent with the density profile of M31 (see e.g. [34, 36, 37] for a $c = 19 - 22$ model of M31).

For the Perseus cluster the observations can be grouped in 3 radial bins by their off-center angle. For each bin we fix

the line position to its average value across Perseus (3.47 ± 0.07 keV). The obtained line fluxes together with 1σ errors are shown in Fig. 2. For comparison, we draw the expected line distribution from DM decay using the NFW profile of [35] (best fit value $r_s = 360$ kpc ($c \approx 5$), black solid line; upper bound $r_s = 872$ kpc ($c \approx 2$), black dashed line). The isothermal β -profile from [38] is shown in magenta. The surface brightness profile follows the expected DM decay line's distribution in Perseus.

Finally, we compare the predictions for the DM lifetime from the two objects. The estimated column density within the central part of M31 ranges between $\bar{\mathcal{S}} \sim 200 - 1000 M_{\odot}/\text{pc}^2$ with the average value being around $600 M_{\odot}/\text{pc}^2$ [24]. The column density of clusters follows from the $c-M$ relation [39–41]. Considering the uncertainty on the profile and that our observations of Perseus go beyond r_s , the column density in the region of interest is within $\bar{\mathcal{S}} \sim 100 - 600 M_{\odot}/\text{pc}^2$. Therefore the ratio of expected signals between Perseus and the center of M31 can be $0.1 - 3.0$, consistent with the ratio of measured fluxes $0.7 - 2.7$.

If DM is made of right-handed (sterile) neutrinos [42], the

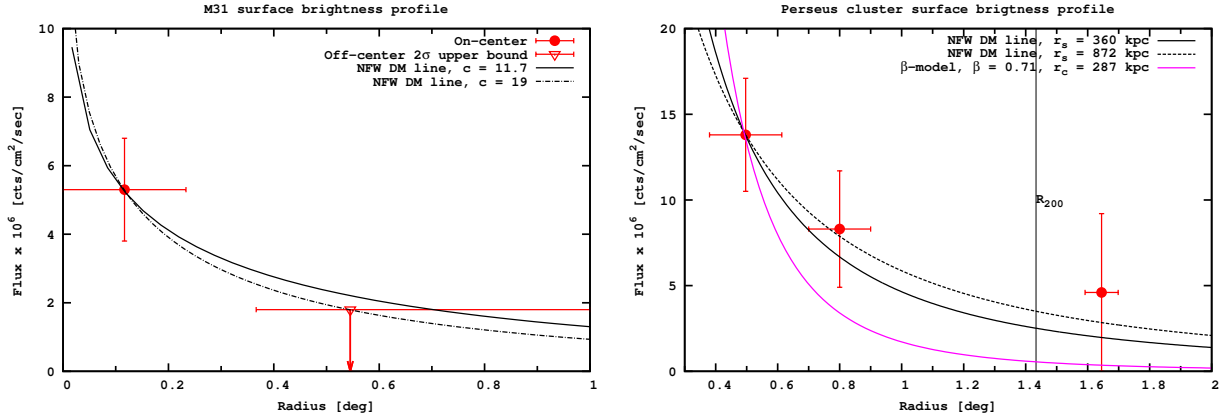


FIG. 2: The line’s brightness profile in M31 (left) and the Perseus cluster (right). A NFW DM distribution is assumed, the scale r_s is fixed to its best-fit values from [34] (M31) or [35] (Perseus) and the overall normalization is adjusted to pass through the left-most point.

lifetime is related to its interaction strength (*mixing angle*):

$$\tau_{\text{DM}} = \frac{1024\pi^4}{9\alpha G_F^2 \sin^2(2\theta) m_{\text{DM}}^5} = 7.2 \times 10^{29} \text{ sec} \left[\frac{10^{-8}}{\sin^2(2\theta)} \right] \left[\frac{1 \text{ keV}}{m_{\text{DM}}} \right]^5.$$

Using the data from M31 and taking into account uncertainties in its DM content we obtain the mass $m_{\text{DM}} = 7.06 \pm 0.06 \text{ keV}$ and the mixing angle in the range $\sin^2(2\theta) = (2-20) \times 10^{-11}$ (taking the column density $\bar{S} = 600 M_{\odot}/\text{pc}^2$ and using only statistical uncertainties on flux we would get $\sin^2(2\theta) = 4.9_{-1.3}^{+1.6} \times 10^{-11}$). This value is fully consistent with previous bounds, Fig. 4. Moreover, it is intriguing that this value is consistent with the result of the paper [18], which appeared when our paper was in preparation. Indeed, our value of $\sin^2(2\theta)$ is based on completely independent analysis of the signal from M31 and our estimates for its DM content, whereas the result of [18] is based on the signal from stacked galaxy clusters and on the weighted DM column density from the full sample.

These values of $\sin^2(2\theta)$ means that sterile neutrinos should be produced resonantly [43–45], which requires the presence of significant lepton asymmetry in primordial plasma at temperatures few hundreds MeV. This produces restrictions on parameters of the νMSM [10].

The position and flux of the discussed weak line are inevitably subject to systematical uncertainties. There are two weak instrumental lines (K $K\alpha$ at 3.31 keV and Ca $K\alpha$ at 3.69 keV), although formally their centroids are separated by more than 4σ . Additionally, the region below 3 keV is difficult to model precisely, especially at large exposures, due to the presence of the absorption edge and galactic emission. However, although the residuals below 3 keV are similar between the M31 dataset (Fig. 1) and the blank sky dataset (Fig. 3), the line is *not detected* in the latter.

If the feature were due to an unmodelled wiggle in the effective area, its flux would be proportional to the continuum

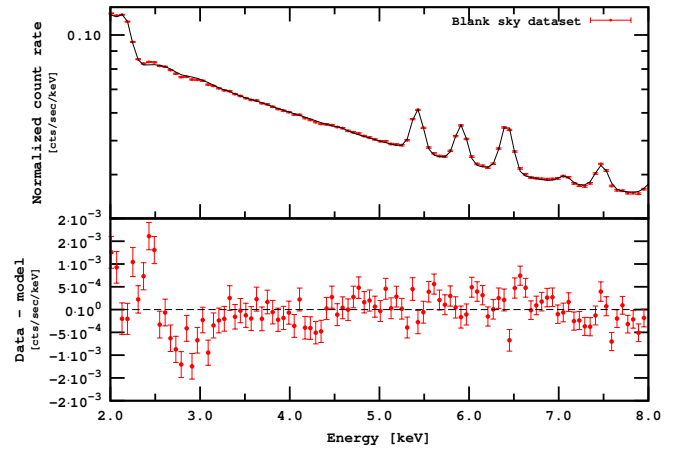


FIG. 3: Combination of 382 MOS blank sky observations.

brightness and the blank-sky dataset would have exhibited a 4 times smaller feature with roughly the same significance (see SOM, Section B). In addition, the Perseus line would not be properly redshifted.

The properties of this line are consistent (within uncertainties) with the DM interpretation. To reach a conclusion about its nature, one will need to find more objects that give a detection or where non-observation of the line will put tight constraints on its properties. The forthcoming *Astro-H* mission [46] has sufficient spectral resolution to spectrally resolve the line against other nearby features and to detect the candidate line in the “strong line” regime [47]. In particular, *Astro-H* should be able to resolve the Milky Way halo’s DM decay signal and therefore all its observations can be used. Failure to detect such a line will rule out the DM origin of the Andromeda/Perseus signal presented here.

Acknowledgments. We thank D. Malyshev for collaboration; A. Neronov for useful critical comments; M. Shaposh-

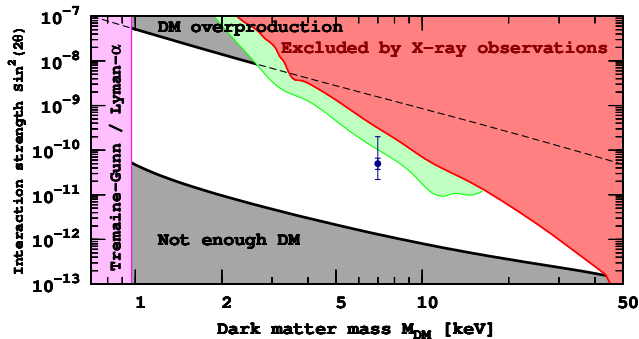


FIG. 4: Constraints on sterile neutrino DM within ν MSM [9]. Recent bounds from [16, 17] are shown in green. Similar to older bounds (marked by red) they are smoothed and divided by factor 2 to account for possible DM uncertainties in M31. In every point in the white region sterile neutrino constitute 100% of DM and their properties agree with the existing bounds. Within the gray regions too much (or not enough) DM would be produced in a minimal model like ν MSM. At masses below ~ 1 keV dwarf galaxies would not form [4, 48]. The blue point would correspond to the best-fit value from M31 if the line comes from DM decay. Thick errorbars are $\pm 1\sigma$ limits on the flux. Thin errorbars correspond to the uncertainty in the DM distribution in the center of M31.

nikov and M. Lovell for reading the manuscript and providing valuable comment. We also thank K. Abazajian, J. Beacom, M. Kaplinghat for their comments. The work of D. I. was supported by part by the the Program of Cosmic Research of the National Academy of Sciences of Ukraine and the State Programme of Implementation of Grid Technology in Ukraine. The work of J.F. was supported by the De Sitter program at Leiden University with funds from NWO. This research is part of the "Fundamentals of Science" program at Leiden University. This research has made use of the NASA/IPAC Extragalactic Database (NED), which is operated by the Jet Propulsion Laboratory, California Institute of Technology, under contract with the National Aeronautics and Space Administration.

- [1] S. Tremaine and J. E. Gunn, Phys. Rev. Lett. **42**, 407 (1979).
- [2] S. D. M. White, C. S. Frenk, and M. Davis, ApJ **274**, L1 (1983).
- [3] S. Hannestad and G. Raffelt, JCAP **0404**, 008 (2004), hep-ph/0312154.
- [4] A. Boyarsky, O. Ruchayskiy, and D. Iakubovskiy, JCAP **0903**, 005 (2009), 0808.3902.
- [5] J. L. Feng, ARA&A **48**, 495 (2010), 1003.0904.
- [6] P. B. Pal and L. Wolfenstein, Phys. Rev. D **25**, 766 (1982).
- [7] K. Abazajian, G. M. Fuller, and W. H. Tucker, Astrophys. J. **562**, 593 (2001), astro-ph/0106002.
- [8] A. D. Dolgov and S. H. Hansen, Astropart. Phys. **16**, 339 (2002), hep-ph/0009083.
- [9] A. Boyarsky, D. Iakubovskiy, and O. Ruchayskiy, Phys. Dark Univ. **1**, 136 (2012), 1306.4954.
- [10] A. Boyarsky, O. Ruchayskiy, and M. Shaposhnikov, Ann. Rev. Nucl. Part. Sci. **59**, 191 (2009), 0901.0011.
- [11] A. Boyarsky, J. Lesgourgues, O. Ruchayskiy, and M. Viel, Phys. Rev. Lett. **102**, 201304 (2009), 0812.3256.
- [12] *The NASA/IPAC Extragalactic Database (NED)*, operated by the Jet Propulsion Laboratory, California Institute of Technology, under contract with the National Aeronautics and Space Administration.
- [13] C. R. Watson, J. F. Beacom, H. Yuksel, and T. P. Walker, Phys. Rev. **D74**, 033009 (2006), astro-ph/0605424.
- [14] A. Boyarsky, D. Iakubovskiy, O. Ruchayskiy, and V. Savchenko, MNRAS **387**, 1361 (2008), arXiv:0709.2301.
- [15] A. Boyarsky, O. Ruchayskiy, M. G. Walker, S. Riemer-Sørensen, and S. H. Hansen, MNRAS **407**, 1188 (2010), 1001.0644.
- [16] C. R. Watson, Z. Li, and N. K. Polley, JCAP **3**, 18 (2012), 1111.4217.
- [17] S. Horiuchi, P. J. Humphrey, J. Oñorbe, K. N. Abazajian, M. Kaplinghat, and S. Garrison-Kimmel, Phys. Rev. D **89**, 025017 (2014), 1311.0282.
- [18] E. Bulbul, M. Markevitch, A. Foster, R. K. Smith, M. Loewenstein, and S. W. Randall, ApJ **789**, 13 (2014), 1402.2301.
- [19] M. J. L. Turner, A. Abbey, M. Arnaud, M. Balasini, M. Barbera, E. Belsole, P. J. Bennie, J. P. Bernard, G. F. Bignami, M. Boer, et al., A&A **365**, L27 (2001), arXiv:astro-ph/0011498.
- [20] L. Strüder, U. Briel, K. Dennerl, R. Hartmann, E. Kendziorra, N. Meidinger, E. Pfeffermann, C. Reppin, B. Aschenbach, W. Bornemann, et al., A&A **365**, L18 (2001).
- [21] *Xmm-newton science analysis system*, <http://xmm.esa.int/sas/>.
- [22] A. M. Read and T. J. Ponman, A&A **409**, 395 (2003), astro-ph/0304147.
- [23] K. D. Kuntz and S. L. Snowden, A&A **478**, 575 (2008).
- [24] A. Boyarsky, O. Ruchayskiy, D. Iakubovskiy, M. G. Walker, S. Riemer-Sørensen, and S. H. Hansen, MNRAS **407**, 1188 (2010), 1001.0644.
- [25] A. De Luca and S. Molendi, Astron. Astrophys. **419**, 837 (2004), astro-ph/0311538.
- [26] *Fin_over_fout public script*, v. 1.1, http://xmm.vilspa.esa.es/external/xmm_sw_cal/background/Fin_over_Fout.
- [27] D. Iakubovskiy, Ph.D. thesis, Leiden University (2013).
- [28] Irby, B., The ftools webpage, HeaSoft, <http://heasarc.gsfc.nasa.gov/docs/software/ftools/ftools.menu.html> (2008).
- [29] J. Nevalainen, M. Markevitch, and D. Lumb, ApJ **629**, 172 (2005), astro-ph/0504362.
- [30] H. Takahashi, Y. Okada, M. Kokubun, and K. Makishima, ApJ **615**, 242 (2004), astro-ph/0408305.
- [31] J. A. Carter and A. M. Read, A&A **464**, 1155 (2007),

- arXiv:astro-ph/0701209.
- [32] D. B. Henley and R. L. Shelton, *Astrophys.J.Suppl.* **202**, 14 (2012), 1208.4360.
- [33] H. Brunner, N. Cappelluti, G. Hasinger, X. Barcons, A. C. Fabian, V. Mainieri, and G. Szokoly, *A&A* **479**, 283 (2008), 0711.4822.
- [34] E. Corbelli, S. Lorenzoni, R. A. M. Walterbos, R. Braun, and D. A. Thilker, *A&A* **511**, A89 (2010), 0912.4133.
- [35] A. Simionescu, S. W. Allen, A. Mantz, N. Werner, Y. Takei, R. G. Morris, A. C. Fabian, J. S. Sanders, P. E. J. Nulsen, M. R. George, et al., *Science* **331**, 1576 (2011), 1102.2429.
- [36] L. Chemin, C. Carignan, and T. Foster, *Astrophys. J.* **705**, 1395 (2009), 0909.384.
- [37] M. A. Sanchez-Conde, M. Cannoni, F. Zandanel, M. E. Gomez, and F. Prada, *JCAP* **1112**, 011 (2011), 1104.3530.
- [38] O. Urban, A. Simionescu, N. Werner, S. W. Allen, S. Ehlert, I. Zhuravleva, R. G. Morris, A. C. Fabian, A. Mantz, P. E. J. Nulsen, et al., *MNRAS* **437**, 3939 (2014), 1307.3592.
- [39] A. Boyarsky, A. Neronov, O. Ruchayskiy, and I. Tkachev, *Phys. Rev. Lett.* **104**, 191301 (2010), 0911.3396.
- [40] L. J. King and J. M. G. Mead, *MNRAS* **416**, 2539 (2011), 1105.3155.
- [41] R. Mandelbaum, U. Seljak, and C. M. Hirata, *JCAP* **0808**, 006 (2008), 0805.2552.
- [42] S. Dodelson and L. M. Widrow, *Phys. Rev. Lett.* **72**, 17 (1994), hep-ph/9303287.
- [43] X.-d. Shi and G. M. Fuller, *Phys. Rev. Lett.* **82**, 2832 (1999), astro-ph/9810076.
- [44] M. Shaposhnikov, *JHEP* **08**, 008 (2008), 0804.4542.
- [45] M. Laine and M. Shaposhnikov, *JCAP* **6**, 31 (2008), arXiv:0804.4543.
- [46] T. Takahashi, K. Mitsuda, R. Kelley, H. Aharonian, F. Aarts, et al. (2012), 1210.4378.
- [47] A. Boyarsky, J. W. den Herder, A. Neronov, and O. Ruchayskiy, *Astropart. Phys.* **28**, 303 (2007), astro-ph/0612219.
- [48] D. Gorbunov, A. Khmel'nitsky, and V. Rubakov, *JCAP* **0810**, 041 (2008), 0808.3910.
- [49] P. Gondoin, B. Aschenbach, C. Erd, D. H. Lumb, S. Majerowicz, D. Neumann, and J. L. Sauvageot, in *X-Ray and Gamma-Ray Instrumentation for Astronomy XI*, edited by K. A. Flanagan and O. H. Siegmund (2000), vol. 4140 of *Society of Photo-Optical Instrumentation Engineers (SPIE) Conference Series*, pp. 1–12.
- [50] M. J. L. Turner, A. Abbey, M. Arnaud, M. Balasini, M. Barbera, E. Belsole, P. J. Bennie, J. P. Bernard, G. F. Bignami, M. Boer, et al., *A&A* **365**, L27 (2001), astro-ph/0011498.
- [51] L. Strüder, U. Briel, K. Dennerl, R. Hartmann, E. Kendziorra, N. Meidinger, E. Pfeffermann, C. Reppin, B. Aschenbach, W. Bornemann, et al., *A&A* **365**, L18 (2001).

Appendix A: Global significance estimate

Significances quoted in the main body of the paper (Table I) reflect the local significance of the signal. Since the position of the line is unknown *a priori* we need to take into account the probability of falsely detecting a statistical fluctuation of equal or higher significance at any position in the entire fitting range (2.0–8.0 keV). In addition, having found a signal in the same energy bin in three separate datasets, we compute this global significance taking into account the probability of such signals showing in the same resolution element by chance. Given the local significance of the signal in each dataset (based on the $\Delta\chi^2$ values and the number of degrees of freedom), and the number of independent resolution elements, we can determine the global significance of the combination of all signals. The number of independent resolution elements, N_E , for our datasets is about 40 (6 keV energy range divided by 150 eV — average energy resolution of the *XMM-Newton*).

The global significance per dataset is computed from the two-sided p-value p_i (directly related to the number of σ of the signal) by multiplying by N_E (see Table II). We took a “two-sided” p-value to take into account both positive and negative residuals.

The combined global significance then is

$$\frac{\prod_i p_i N_E}{N_E^{N_d-1}} = 1.1 \cdot 10^{-5} \quad (\text{A1})$$

where $N_d = 3$ is the number of datasets. This corresponds to a false detection probability for the combination dataset of **0.0011%**. Converted to the significance this p-value gives 4.4σ **global significance**.

Alternatively, we could have taken into account only probability of positive fluctuations (so “two-sided” p-values in the Table II should be divided by 2). Using the same formula (A1) we would obtain 4.7σ global significance.

Introducing systematic uncertainties into all our datasets at the level of $\sim 1\%$, the local significances drop by about 1σ each.

Dataset	$\Delta\chi^2$	d.o.f.	local significance	local p-value	false detection probability	global significance
M31-oncne (MOS)	13	2	3.18σ	$1.5 \cdot 10^{-3}$	0.06	1.89σ
Perseus (MOS)	9.1	2	2.56σ	$1.05 \cdot 10^{-2}$	0.42	0.81σ
Perseus (PN)	8	2	2.36σ	$1.83 \cdot 10^{-2}$	0.73	0.35σ
All combined					$1.1 \cdot 10^{-5}$	4.4σ

TABLE II: Table of significances per dataset. Quoted p-values refer to the two-sided case (one-sided p-values are half of the two-sided ones). The false detection probability refers to the probability of falsely detecting a signal in that dataset like the one under consideration or stronger at any energy in the range considered. The global significance was converted from the false detection probability per dataset. The combined false detection probability and global significance of these three datasets is also given (computed from the individual detections, not from a single combined dataset).

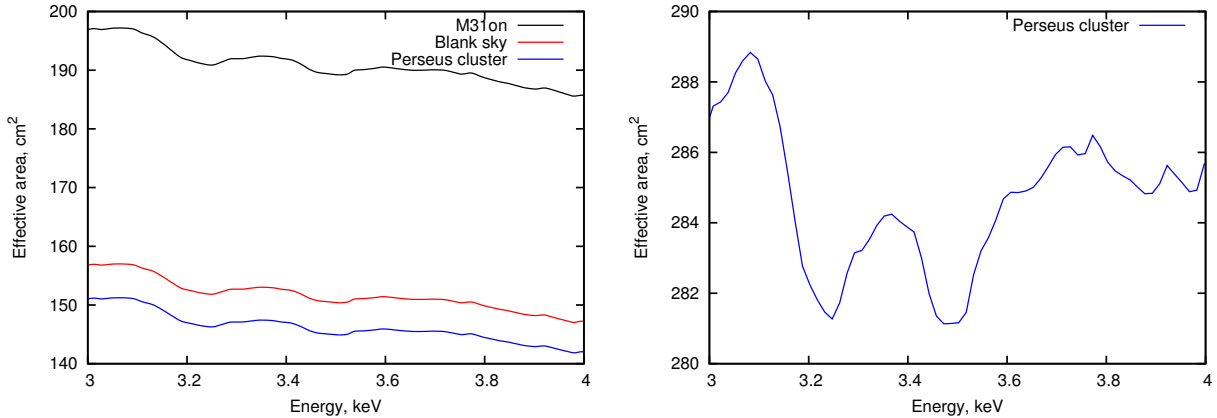


FIG. 5: Exposure averaged effective area of the XMM MOS camera for the combination of observations of Perseus galaxy cluster, M31 and blank-sky (*left panel*). For Perseus galaxy cluster we also show the exposure averaged PN camera's effective area (*right panel*).

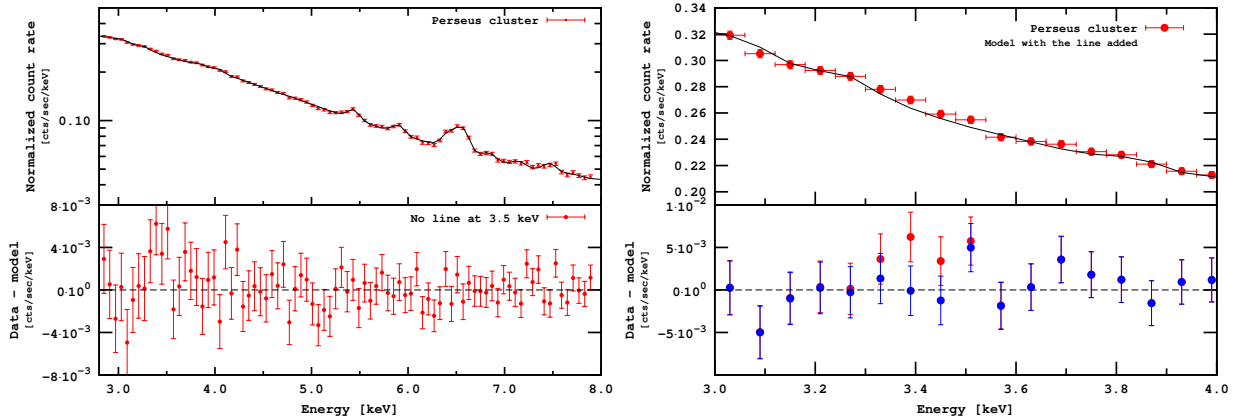


FIG. 6: *Left*: Folded count rate (top) and residuals (bottom) for the combined spectrum of 16 observations of MOS cameras (listed in the Tabel III) of the Perseus cluster. Statistical Y-errorbars on the top plot are smaller than the point size. The line around 3.5 keV is *not added*, hence the group of positive residuals. *Right*: zoom onto the line region. The spectrum is shown in the detector restframe, therefore the line is shifted left according to the Perseus redshift.

Appendix B: Effective area

In this Appendix we show the effective area of the Perseus, M31 and blank-sky datasets (Fig. 5). One sees that all three datasets exhibit a (known) wiggle at energy $E \sim 3.5$ keV in the detector frame (about 1.5% deviation from the monotonic behaviour). This kind of behavior of the effective area is due to K-, L- and M-shell transitions of Al, Sn and Au. The SAS software uses calibration files based on ray-tracing calculations through numerical models of the telescope assemblies [49–51]. The effective

	ObsID	Off-axis angle arcmin	Cleaned exposure MOS1/MOS2 [ksec]	FoV [arcmin ²] MOS1/MOS2	$F_{in}-F_{out}$
1	0305690301	22.80	18.6 / 18.6	473.6 / 574.3	1.266 / 1.340
2	0085590201	25.01	40.1 / 40.5	564.6 / 572.1	1.290 / 1.336
3	0204720101	27.87	14.1 / 14.5	567.7 / 574.5	2.373 / 2.219
4	0673020401	29.48	15.6 / 17.6	479.6 / 574.0	1.318 / 1.331
5	0405410201	29.52	16.1 / 16.6	480.8 / 573.9	1.354 / 1.366
6	0305690101	29.54	25.1 / 25.4	476.0 / 573.5	1.231 / 1.247
7	0405410101	31.17	15.8 / 16.8	481.8 / 572.9	1.235 / 1.195
8	0305720101	31.23	11.5 / 11.8	476.8 / 573.9	1.288 / 1.296
9	0673020301	36.54	13.9 / 15.4	485.4 / 573.8	1.211 / 1.304
10	0305690401	36.75	25.9 / 26.0	479.1 / 573.8	1.158 / 1.156
11	0305720301	41.92	16.7 / 17.5	464.7 / 573.6	1.433 / 1.447
12	0151560101	47.42	23.7 / 23.6	572.1 / 573.6	1.294 / 1.206
13	0673020201	53.31	22.8 / 23.4	479.5 / 573.9	1.262 / 1.228
14	0204720201	54.11	22.4 / 22.9	564.0 / 573.2	1.153 / 1.195
15	0554500801	95.45	15.0 / 15.3	480.8 / 572.7	1.098 / 1.113
16	0306680301	101.88	12.3 / 13.0	468.1 / 574.0	1.177 / 1.089

TABLE III: Parameters of the *XMM-Newton* spectra of the Perseus cluster used in our analysis. The observations are sorted by the off-axis angle from the center of the Perseus cluster. Two central observations (ObsIDs 0305780101 and 0085110101) were not included in the analysis to avoid modeling of the emission from the core of the Perseus cluster. Notice that only these two central observations were used in [14], therefore our dataset and that of [14] is independent from each other. The difference in FoVs between MOS1 and MOS2 cameras is due to the loss CCD6 in MOS1 camera. The parameter $F_{in}-F_{out}$ (last column) estimates the presence of residual soft protons according to the procedure of [21]. Note, however, that for the bright extended sources, such an estimate is not appropriate, see http://xmm2.esac.esa.int/external/xmm_sw_cal/background/epic_scripts.shtml for details). Horizontal lines show how we group observations for building the surface brightness profile of the line (as shown in Fig. 2, right panel in the main text).

Range of offsets	Exposure [ksec]	Flux [cts/sec/cm ²]
23 – 37'	400	13.8 ± 3.3
42' – 54'	230	8.3 ± 3.4
96' – 102'	56	4.6 ± 4.6

TABLE IV: Definitions of the radial bins used for the data analysis of the Perseus cluster.

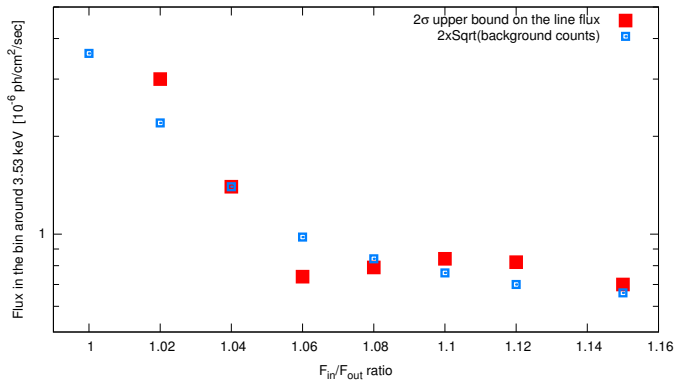


FIG. 7: The dependence of the 2σ upper bound on the flux in the blank sky dataset on the imposed $F_{in} - F_{out}$ criterion. The statistical error on this parameter is about 5%. The bound on the flux remains at the quoted level until we start to lose significant fraction of observations for $F_{in} - F_{out} < 1.06$. Blue squares are defined as $2 \times \sqrt{N_{bg}}$ where N_{bg} is the number of background counts in the energy bin, equal to spectral resolution. The difference between blue and red squares appears because spectral modeling takes into account also the line shape.

area curves differ between datasets mostly due to the vignetting effect, which depends on energy and on the weighting during the data stacking.

Looking at the left panel of SOM Fig. 2 one sees that the effective area of all MOS observations is self-similar. The variation in shape between three datasets in the energy range 3.4-3.6 keV is less than 0.1% and less than 0.4% in the 3-4 keV range. If the line is due to an unmodeled wiggle, this would mean that a 10 times larger unmodeled feature (line is 3-4% of the continuum level) is present in the datasets of M31 and Perseus, but *not* in the blank sky. As all datasets are combinations of observations taken over long period of lifetime of the XMM, the existence of such a feature is difficult to imagine.

Notice that if this wiggle would be the cause of the signal, reported in this paper, it would fail to explain why the redshift of the line in the Perseus cluster is correctly detected (at energies $3.5/1+z = 3.4$ keV the effective area has a local maximum, rather than minimum). It would also fail to explain the detection of the line in the combined dataset of 70 clusters at different redshifts, presented in [18].

Additionally, if the feature is due to an *unmodelled* wiggle in the effective area, its flux in each dataset should be proportional to the continuum brightness. Comparing the M31 and blank-sky datasets we see that the count rate at energies of interest is 4 times larger for M31, so that the blank-sky dataset would have exhibited a 4 times smaller (instrumental) feature with a flux $\sim 1.2 \times 10^{-6}$ cts/sec/cm², were it due to a wiggle in the effective area. Notice that the exposure for the blank sky is 16 times larger and such a line would have been resolved with sufficient statistical significance. The upper (non-detection) limit from the blank-sky dataset is ~ 2 lower (0.7×10^{-6} cts/sec/cm²).

Appendix C: Flare removal

In this Section we investigate how sensitive the derived bounds are to the imposed $F_{in} - F_{out}$ cut. To this end we have imposed a number of different cuts in $F_{in} - F_{out}$ and rederived the 2σ upper bound in the blank sky dataset. We see (Fig. 7) that the bound derived in the paper does not really change until we start to impose very stringent cuts $F_{in} - F_{out} < 1.06$, which starts to drastically reduce the statistics (clean exposure) as the blue squares in Fig. 7 demonstrate).

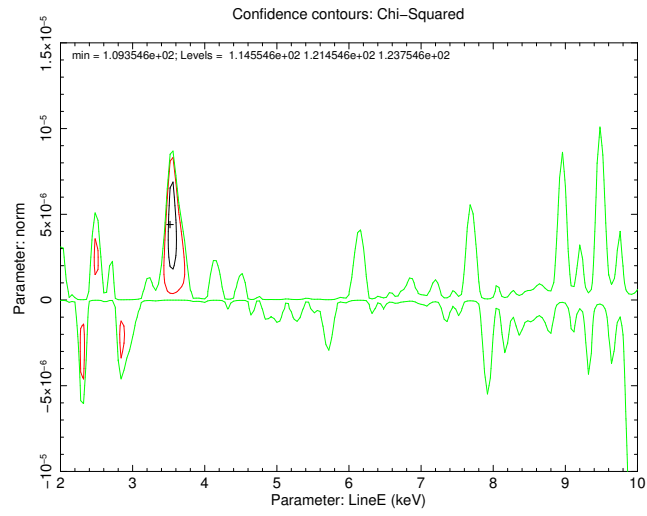


FIG. 8: Structure of the residuals (both positive and negative) around the best fit model for M31 central observation. Red contours show residuals that are above 1σ . Black contour shows more than 3σ residual (3.53 keV line). The other residuals are below 1σ .

	ObsID	Off-axis angle	Cleaned exposure		FoV [arcmin ²]	$F_{in}-F_{out}$
		arcmin	MOS1/MOS2 [ksec]	MOS1/MOS2		
1	0405320501	0.02	12.3/13.6	480.6/573.2	1.132/1.039	
2	0405320701	0.02	14.8/14.9	480.7/572.8	1.046/1.057	
3	0405320801	0.02	13.1/13.1	488.2/573.0	1.160/1.117	
4	0405320901	0.02	15.5/15.6	488.0/574.3	1.099/1.065	
5	0505720201	0.02	25.2/26.2	485.6/572.1	1.079/1.057	
6	0505720301	0.02	25.4/24.3	486.0/573.9	1.129/1.105	
7	0505720401	0.02	19.9/20.2	488.6/573.1	1.113/1.108	
8	0505720501	0.02	12.9/13.9	480.3/574.1	1.151/1.064	
9	0505720601	0.02	20.2/20.4	488.3/571.4	1.085/1.108	
10	0551690201	0.02	20.5/20.3	486.5/574.2	1.099/1.072	
11	0551690301	0.02	19.7/19.4	479.3/573.0	1.109/1.117	
12	0551690501	0.02	16.9/18.4	486.3/573.2	1.095/1.109	
13	0600660201	0.02	17.4/17.5	487.0/572.9	1.080/1.041	
14	0600660301	0.02	16.1/16.1	488.6/572.0	1.054/1.041	
15	0600660401	0.02	15.0/15.5	479.9/573.1	1.078/1.072	
16	0600660501	0.02	13.5/14.3	488.2/573.4	1.079/1.083	
17	0600660601	0.02	15.2/15.1	481.8/573.6	1.073/1.041	
18	0650560201	0.02	21.0/21.3	488.1/573.3	1.198/1.140	
19	0650560301	0.02	26.9/29.0	487.9/572.6	1.082/1.095	
20	0650560401	0.02	12.4/13.5	488.0/573.1	1.157/1.069	
21	0650560501	0.02	15.8/21.6	487.8/573.4	1.162/1.114	
22	0650560601	0.02	20.8/21.5	487.5/572.2	1.085/1.068	
23	0674210201	0.02	19.6/19.6	478.6/573.3	1.094/1.083	
24	0674210301	0.02	14.9/15.0	488.1/573.6	1.052/1.043	
25	0674210401	0.02	17.9/18.1	485.7/572.7	1.071/1.081	
26	0674210501	0.02	16.2/16.3	488.8/573.5	1.192/1.139	
27	0202230201	1.44	18.3/18.4	567.1/572.8	1.089/1.108	
28	0202230401	1.44	17.0/17.1	566.5/573.6	1.118/1.109	
29	0202230501	1.44	9.2/9.4	568.1/574.1	1.048/1.129	
30	0402560201	23.71	16.0/16.6	478.7/574.0	1.096/1.095	
31	0505760201	23.71	35.2/38.6	476.6/571.6	1.065/1.058	
32	0511380201	23.71	15.3/15.4	485.0/572.7	1.126/1.047	
33	0511380601	23.71	14.8/17.2	485.4/573.1	1.041/1.074	
34	0402560901	24.18	42.4/42.9	475.0/572.8	1.118/1.071	
35	0672130101	24.24	73.0/78.6	473.1/572.8	1.088/1.064	
36	0672130501	24.24	22.7/25.4	477.0/574.8	1.097/1.110	
37	0672130601	24.24	67.8/67.3	471.8/571.4	1.115/1.101	
38	0672130701	24.24	70.7/74.3	484.8/573.5	1.076/1.052	
39	0410582001	26.29	13.2/13.9	485.4/575.0	1.073/1.030	
40	0402561001	28.81	48.0/49.4	478.4/572.5	1.084/1.042	
41	0402560301	30.34	43.9/45.7	474.6/573.1	1.037/1.027	
42	0505760301	39.55	41.0/41.3	485.0/570.8	1.022/1.022	
43	0402561101	39.56	44.8/44.8	478.7/571.4	1.121/1.067	
44	0404060201	42.94	19.1/19.1	480.7/573.7	0.993/1.045	
45	0402561201	47.37	38.1/39.2	478.5/573.3	1.077/1.034	
46	0402560501	49.06	48.8/50.6	487.2/572.9	1.102/1.079	
47	0511380301	49.06	31.5/31.0	482.0/572.3	1.105/1.082	
48	0151580401	50.89	12.3/12.3	567.2/574.1	1.131/1.020	
49	0109270301	55.81	25.5/25.0	562.6/571.6	1.110/1.106	

TABLE V: Parameters of the *XMM-Newton* spectra of M31 used in our analysis. The significant difference in FoVs between MOS1 and MOS2 cameras is due to the loss CCD6 in MOS1 camera. The $F_{in}-F_{out}$ parameter estimating the presence of residual soft protons according to procedure of [21] is also shown. First 29 observations are the dataset M31 ON, the remaining 20 – the dataset M31 OFF.